Journal of Nondestructive Evaluation (2022) 41:27
https://doi.org/10.1007/s10921-022-00858-1

Model-Based POD Evaluation with Parameters from Experiment: A Comparative Study of TMR and Coil Array Probes

Kai Sun[1,3] · Yu Tao[1,3] · Xinchen Tao[1,3] · Yunze He[2] · Chaofeng Ye[1,3]

Received: 14 July 2021 / Accepted: 14 February 2022 / Published online: 8 March 2022
© The Author(s), under exclusive licence to Springer Science+Business Media, LLC, part of Springer Nature 2022

Abstract
Aiming at better sensitivity, higher efficiency and lower cost, a variety of eddy current testing (ECT) probes have been developed for steam generator tube (SGT) inspection. Magnetoresistance sensors emerge as a promising alternative to coils due to their advantages of fine spatial resolution and high sensitivity over a wide frequency range. However, it still lacks quantitative comparison between the probes. This paper proposes a quantitative comparison of tunnel magnetoresistance (TMR) array probe and coil array probe for SGT inspection. Based on repeated experiments, probability of detection (POD) curves of the probes are calculated. It is found that the TMR array probe is superior for inspection of axially oriented defects. For circumferential inner diameter defects, the POD of the TMR array probe is lower than the coil array probe. In addition, this paper proposes a model-based POD calculation method with parameters obtained from experiment to compare the probes. Only one defect is repeatedly inspected experimentally. Then the distribution characteristics of the experimental results are calculated. These parameters are applied to calibrate numerical results and to generate probability distribution features. Lastly, POD curves are calculated from the experiment and simulation data. The method is validated by comparing the calculated POD curves of the array probes to the experimental POD curves, with average error 1.04% and 0.66% for the TMR array probe and coil array probe, respectively. This method can be employed to compare different probes and optimize parameters of a probe efficiently and economically in the future.

Keywords Eddy current testing · TMR · Array probe · POD · Tube inspection

1 Introduction

Steam generator of a nuclear power plant consists of thousands of heat transfer tubes, which transfer energy from the primary side of nuclear reaction contaminated with radioactive materials to the circulating water of the secondary side. Periodically inspection of steam generator tube (SGT) is significant in ensuring nuclear power plant safety [1]. Eddy current testing (ECT) is a widely used nondestructive testing (NDT) technology. Over the past decades, different kinds of ECT probes have been developed for SGT inspection, such as bobbin probe, rotating probe, X-probe [2] and array probe, etc. Bobbin probe can scan fast and has excellent sensitivity for axial oriented defects, but it has limited detectability to circumferential cracks. Moreover, it is difficult for a bobbin probe to identify multiple defects that are located at the same axial position. Rotating probe such as pancake probe and plus point probe [3] has better performance for defect quantification than bobbin probe. However, as mechanically rotating is required, the inspection speed of a rotating probe is limited, and the probe is prone to wear. One faster solution is to use probe with array coils/sensors, in which multiple coils/sensors are arranged as an array to image the testing sample [4–6]. Zhao Y et al. proposed an array ECT probe of high efficiency and detectability. The excitation unit of the probe contains large coils of spiral configuration, and the pick-up unit consists of four small pancake coils with rectangle arrangement [7]. A novel weak coupling sensing structure of pulsed eddy current was proposed in [8]. In [9], a flexible arrayed eddy current sensor was developed to improve the reliability of testing the hollow axle inner surfaces. To fur-

✉ Chaofeng Ye
yechf@shanghaitech.edu.cn

1 School of Information Science and Technology, ShanghaiTech University, Shanghai 201210, China

2 College of Electrical and Information Engineering, Hunan University, Changsha 410082, China

3 Shanghai Engineering Research Center of Energy Efficient and Custom AI IC, Shanghai 201210, China

ther improve the spatial resolution and operating frequency range, hybrid ECT probes including excitation coils and magnetic field sensors have been developed [10–12]. Tunnel magnetoresistance (TMR) sensor is a kind of magnetic sensor based on quantum mechanics, in which electrons tunnel through an insulating layer. The resistance of a TMR sensor depends on the applied magnetic field. TMR sensor has advantages of high sensitivity, low power consumption and small aging deterioration. As the size of a TMR sensor can be very small, ECT probe with TMR sensors can obtain magnetic field image with high spatial resolution. An eddy current probe with integrated TMR sensors for SGT inspection was proposed in [13]. Experimental results demonstrated the feasibility of the concept and validated that the probe has excellent ability to detect various defects.

Viewing those different kinds of probes, it is valuable to compare their performances in quantitative manner for making a proper choice in application. Reliability of a NDT tool is a key parameter in evaluation of the effeteness of the probe [14–16]. The most common metric for evaluation of NDE techniques is probability of detection (POD), which describes the likelihood of correctly identifying a defect, and the probability of false alarm (PFA), which describes the probability of labelling a good area as defective [17]. Traditionally, POD evaluations are entirely empirical, where flaw signals and their variability are determined using large number of experimental measurements from different samples. The experimental data are used to estimate the POD of the NDT tool. Unfortunately, the determination of the POD based on this method requires a rather extensive set of measurements to obtain statistically sound estimates. In general, this approach for generating POD curves is time consuming and expensive [18], as it requires manufacture of a large number of defective samples. Due to cost and time cycle pressures, the NDT industry is trying to use simulated results instead of experimental data to estimate POD curves [19, 20]. The POD curve generated by simulation can avoid the time-consuming and laborious, high cost and high cycle of experimental activities. Several authors refer to the NDT simulation concerning POD curves as MAPOD (model assisted POD) [21]. However, the results of these numerical methods typically have a certain deviation from the experimental results.

This paper proposes a quantitative performance evaluation framework for comparison of array probes for SGT inspection based on POD calculation. Section 2 shows the concept and theoretical background of POD calculation. In Sect. 3, the TMR array probe and coil array probe, as well as experimental results for SGT are presented. POD curves are calculated based on experimental results, and the detection capabilities of the two probes are compared. In Sect. 4, a calculation method of POD curves based on simulation model and experimental data is proposed. The proposed method only requires repeated detection of one defect to obtain the parameters for POD curves calculation. The discussion and conclusion follow in Sect. 5 and Sect. 6.

2 Principle

A POD curve relates the likelihood of detection to a characteristic parameter (a) of a defect [22]. Therefore, POD is written as a function of a. Assuming the response of the defect with characteristic parameter a is $\hat{a}$, POD can be obtained from the relation between a and $\hat{a}$. To simplify the discussion, it is assumed that $\hat{a}$ is a function of a as written in Eq. (1).

$$\widehat{a} = f(a) + \delta. \tag{1}$$

Here f is a transfer function from a to $\hat{a}$, which should be chosen properly to meet the calculation requirements [22–24]. δ is the measurement error and it follows a distribution with zero mean and constant standard deviation τ. When making decisions, the defect is detected if the $\hat{a}$ exceeds the predefined decision threshold $\hat{a}_{dec}$. The POD is generated by calculating the probability of the signal response exceeds the decision threshold and shown as Eqs. (2) and (3).

$$\mathrm{POD}(a) = \mathrm{Probability}(\widehat{a} > \widehat{a}_{dec}), \tag{2}$$

$$\mathrm{POD}(a) = 1 - \Phi\left\{\frac{\widehat{a}_{dec} - f(a)}{\tau}\right\}, \tag{3}$$

where Φ is a cumulative normal distribution function. The mean value and standard deviation of Φ can be estimated by the maximum-likelihood estimation method to achieve the best fitting to the experimental data.

The threshold $\hat{a}_{dec}$ is selected using an appropriate criterion [25]. Following criteria may be used to select the threshold.

2.1 Set PFA to a Constant

In many applications, it is desired to keep the PFA as low as possible. The PFA is independent of the probability density function (PDF) of the flaw signal and only depends on the PDF of the background noise. The threshold is selected so that the PFA is a constant.

2.2 Set POD of the Critical Flaw Size to a Constant

This scheme is useful when the inspection system is expected to detect flaws that are bigger than a critical size. The threshold is chosen so that the critical flaw is detected with a specified POD.

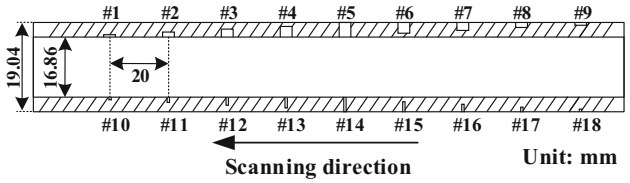

Fig. 1 Diagram of the defects in the tube wall of the SGT sample

3 POD Based on Experiment

Two array probes for SGT inspection, namely TMR array probe and coil array probe are investigated experimentally. The tested sample is an SGT with EDM machined defects. The material of the tube is Inconel alloy 690. The dimensions of the tube are specified in Fig. 1. Eighteen defects were machined on the tube wall (TW). The defect #1 to #9 are axial notches, among which #1 to #4 are inner diameter (ID) notches, #5 is through wall notch and #6 to #9 are outer diameter (OD) notches. The length and width of the defects are 2.54 mm and 0.127 mm, respectively. The depths of the defects from left to right are 20% (ID), 40% (ID), 60% (ID), 80% (ID), 100%, 80% (OD), 60% (OD), 40% (OD), 20% (OD) of the TW, respectively. The defect #10 to #18 are circumferential notches with similar dimensions as the axial notches. The manufacturing tolerance is ± 0.05 mm.

3.1 Probe Design

3.1.1 TMR Array Probe

An eddy current probe with integrated array TMR sensors for SGT inspection was developed. The TMR sensors were wire bonded on a circular PCB, as shown in Fig. 2. The sensing directions of the sensors were placed along the radius of the circular board, in which way the radial component of the magnetic field ($\boldsymbol{B_r}$) was measured. The probe consists of 32 sensors. The TMR array sensors were placed inside a 3D printed plastic structure. A cylindrical coil was wounded outside of the sensors, in which alternating current was driven to induce eddy current in the TW. The OD, ID, height and number of turns of the coil were 16 mm, 15.8 mm, 8 mm and 200 respectively. The array TMR sensors were placed in the center of the coil. More details of the TMR probe can be found in [13]. The probe can work in a wide temperature range from − 40 to 80°C and can work normally in a steam generator of nuclear power plant. However, the long-term stability of the probe in a radiation environment has not been tested yet.

3.1.2 Coil Array Probe

The coil array probe consists of two rows of coils. Each row has 16 coils that cover the full circumference of the inner tube. The inner and OD of the coils are 0.5 mm and 2.6 mm respectively. The height of the coils is 0.5 mm. The spacing between the two rows is 6 mm. The OD of the array is 16 mm. The probe works in transmit-receive mode, e.g., at each time, a coil carrying AC current is activated as a transmitter, and three other coils are selected as receivers picking up the magnetic field. Multiplexers are used to switch on different coils at different time slots. The axial channels are obtained by transmitting from coil A(n) to B(n) and B(n + 1), which are noted as Coil-A in following context. The circumferential channels are obtained by transmitting from A(n) to A(n + 1), which are noted as Coil-C. Here n is an integer ranging from 1 to 16, and coil A17 is the coil A1 and coil B17 is the coil B1 (Fig. 3).

3.2 Experiment Setup

The experimental system is shown in Fig. 4. The data collection is controlled by a computer, which controls a gantry system pulling the probe scanning inside the tube. The move speed is 1 mm/s, and step size is 0.5 mm. A sinusoid voltage is generated by a signal generator (NI PXIe-5413 module) and is connected to the excitation coil. The outputs of the array sensors are multiplexed and then amplified, details about the circuits can be found in [5] and [13]. The switching time of the multiplexers is less than 1 μs. Considering the circuit's low-pass filter and the software delay, each probe requires about 10 ms to obtain a set of signals from all the sensors. A data acquisition card (NI PXIe-5753) is used to digitalize the output signal of the probes. The address signal of the multiplexer is also generated by this module during the inspection. Lastly, the magnitudes and phases of the sinusoidal signals are calculated with a LabVIEW VI. The reference signal was obtained from the excitation voltage.

3.3 Raw Experimental Images

The tube sample was scanned by the TMR array probe and coil array probe separately. The frequencies of the probes were optimized by sweeping the frequency of each probe and the frequency with the best defects' indications were utilized in the experiment. For the TMR array probe, the frequency of the excitation current was set to 30 kHz. The raw images of the TMR array probe are presented in Fig. 5. It is seen that most of the defects are observable from the images. The signal amplitudes of the axial defects are an order higher than that of the circumferential defects indicating that the probe is more sensitive to the axial defects. This is because the eddy current induced by the excitation coil of the probe flows

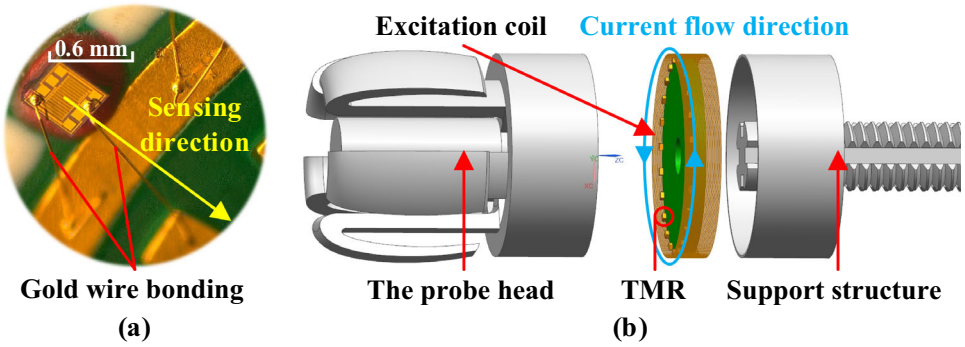

Fig. 2 **a** Picture of the TMR sensors bonded on a circular PCB and **b** diagram of the TMR array probe [13]

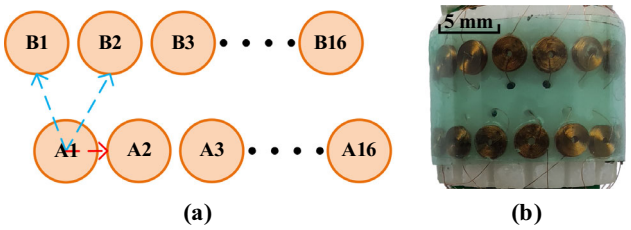

Fig. 3 **a** Schematic diagram and configuration of the three channels of the coil array probe, and **b** photograph of the coil array probe

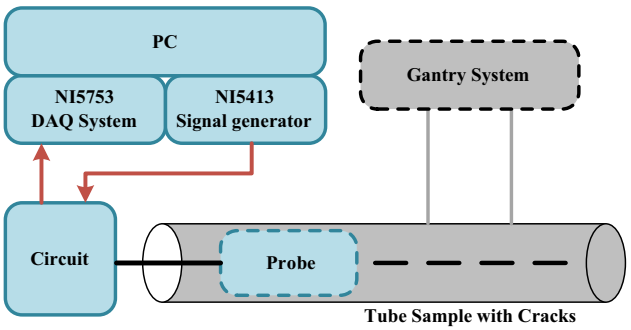

Fig. 4 Diagram of the experiment system

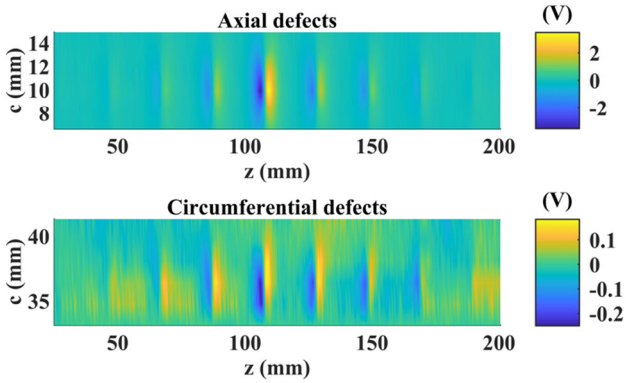

Fig. 5 Experimental results: real component of the TMR sensors' output

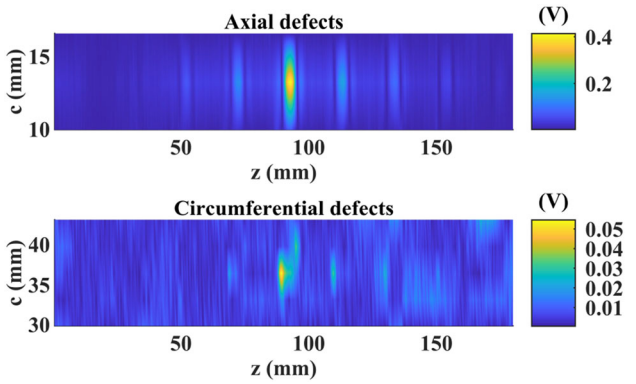

Fig. 6 Experimental results: amplitude of the axial channels (Coil-A) of the coil array probe

circumferentially in the TW, which will be disturbed much more significantly by an axial oriented defect compared with a circumferential oriented defect. It should be noted that the images in Fig. 5 were obtained simultaneously in a single probe pass. Due to the difference in signal amplitude, they are plotted in separate plots with different color bars to show the smaller signals more clearly.

The TMR sensors' outputs are proportional to the magnetic field. Unlike this, the outputs of the coils are proportional to the differential of the magnetic field to time. Therefore, the optimum operating frequency of the coil array probe is much higher than the TMR array probe. Since the effect of frequency is affected by the characteristics of the coils that are used to construct the probe, the optimum frequency may differ for different probes. For the coil array probe used in this study, the operating frequency was set to 300 kHz. The penetration depth of eddy current is inversely proportional to the square root of the excitation frequency. So, the frequency should not be too high, and the penetration depth of the TMR probe is larger than the coil array probe. The raw images of the coil array probe are depicted in Figs. 6 and 7, where Fig. 6 shows the outputs of the axial channels (Coil-A) and Fig. 7 presents the images of the circumferential channels (Coil-C). It is seen that the axial defects are more clearly observed in the axial channels. The circumferential channels are more sensitive to circumferential defects. The images were obtained in a single probe pass but plotted separately.

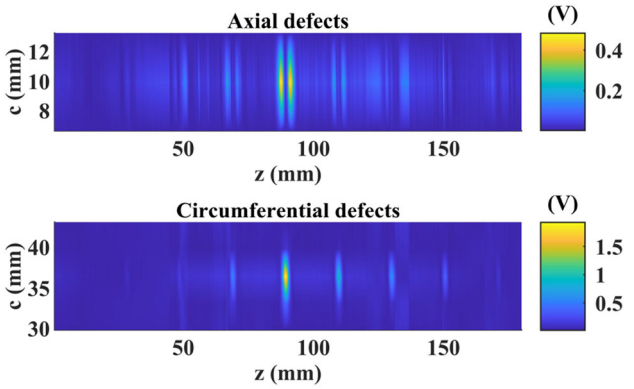

Fig. 7 Experimental results: amplitude of the circumferential channels (Coil-C) of the coil array probe

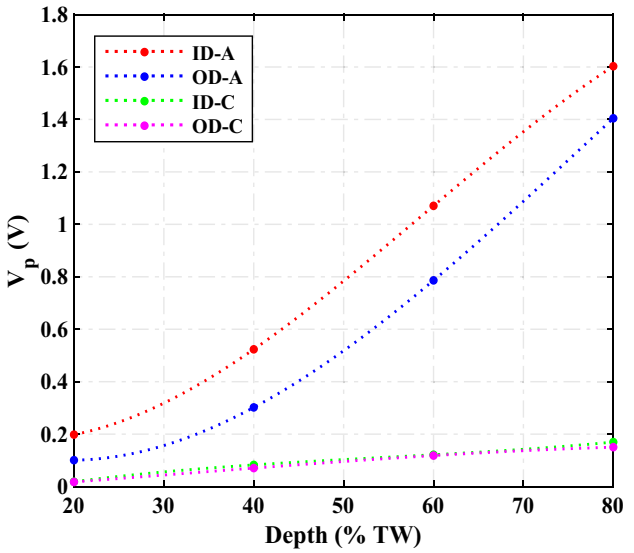

Fig. 8 Experimental results: mean values of V_p versus defect depth for the TMR array probe

3.4 Repeat of the Experiment and Analysis

To evaluate the reliability of the probes, the experiments were repeated 30 times with multiple sets of output images obtained. Then, the mean value and variance of the peak signal of the defects (V_p) were analyzed. Figures 8, 9 and 10 present the mean values of V_p of the TMR array probe, Coil-A and Coil-C of the coil array probe respectively, where ID-A, OD-A, ID-C, OD-C refer to the axial defects located on ID of TW, axial defects located on OD of TW, circumferential defects located on ID of TW and circumferential defects located on OD of TW respectively.

It is seen that with the increase of defect depth, the mean value of the signal becomes larger. The variances of V_p calculated based on the repeated experiments are presented in Fig. 11, where the variances of ID-A defects with depths varying from 40 to 80% of the TW are shown. It is seen

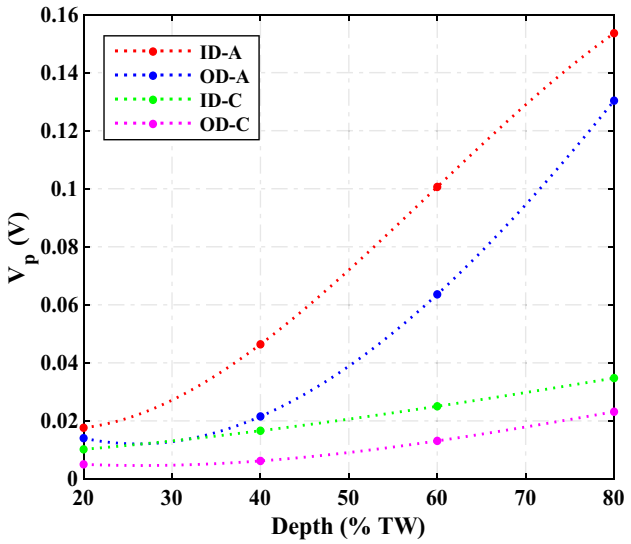

Fig. 9 Experimental results: mean values of V_p versus defect depth for Coil-A of the coil array probe

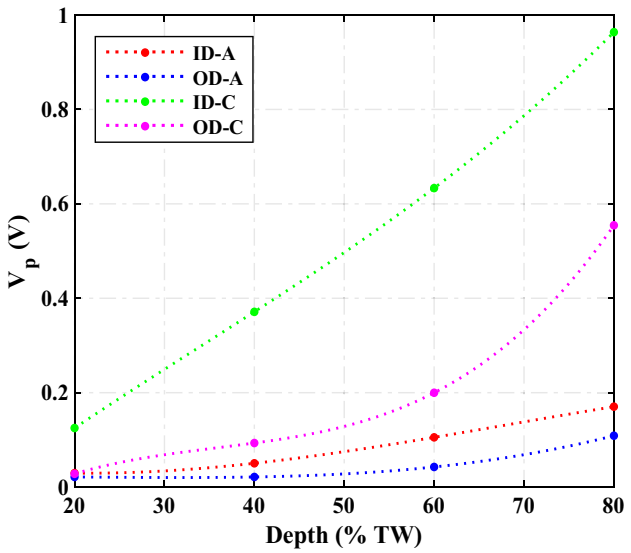

Fig. 10 Experimental results: mean values of V_p versus defect depth for Coil-C of the coil array probe

that V_p is positively correlated with the defect depth. The variation of the V_p is small compared with its mean value, which is reasonable considering the fact that all the experimental conditions were kept the same during the repeated experiments. Therefore, the variance of a certain kind of defect can be approximately considered to be the same. So, the distribution characteristics calculated from the repeated experimental results of a defect can be applied to the numerical results for POD calculation.

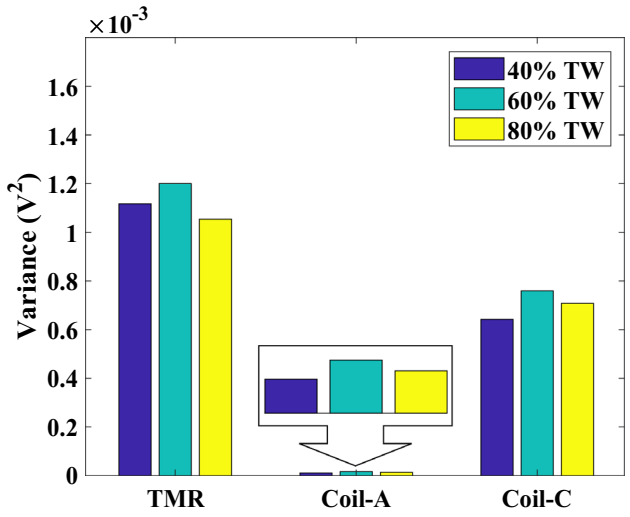

Fig. 11 Variances of V_p of three ID-A defects with different depths measured with the TMR array probe and the coil array probe

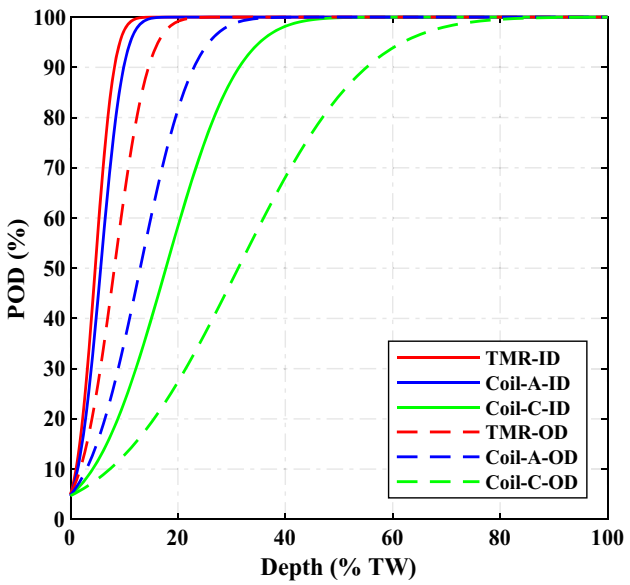

Fig. 12 POD curves of axial defects calculated based on the experimental data

3.5 POD Curves Based on Experimental Data

To simplify the POD calculation, the transfer function (f) of the output voltage versus defect depth are approximately linearly fitted. To facilitate comparison, the detection threshold of each probe was chosen by setting PFA = 5%. POD curves of the probes calculated with Eq. (3) are shown in Figs. 12 and 13.

It is seen from Fig. 12 that for axial defects located on the ID of the tube, the POD curve of the TMR array probe is uppermost. The POD curve of the axial channel of the coil array probe is close to the curve of TMR array probe and

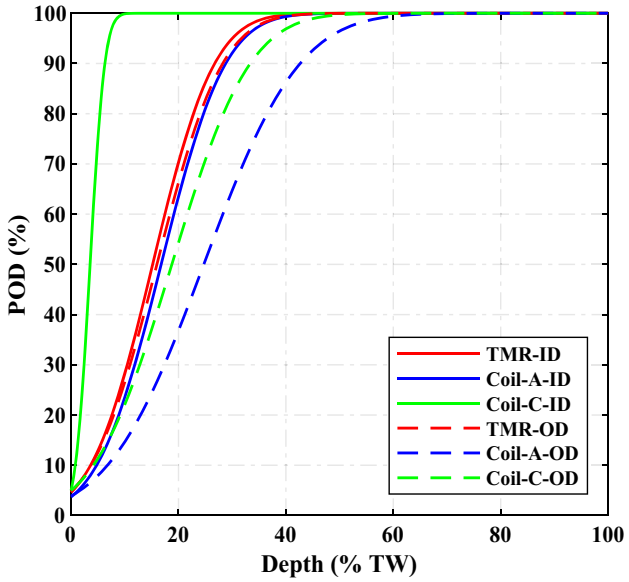

Fig. 13 POD curves of circumferential defects calculated based on the experimental data

both probes can reach more than 90% of POD for defects with depth greater than 10% TW. It is a well-known fact that the axial channel of a coil array probe is much more sensitive to axial defects than the circumferential channel. For the axial defects located on the OD of the tube, the POD curve of the TMR array probe is higher than the curves of the coil array probe. Taking the OD defect with depth 10% TW as an example, the POD of the TMR array probe is 64%, while the POD of the coil array probe is only 35%. Consequently, it concluded that the TMR array probe has better performance for detecting axial OD defects than the coil array probe.

It is seen from Fig. 13 that for circumferential ID defects, the POD curve of the circumferential channel of the coil array probe is at the top, 100% detection probability can be achieved for defect with depth 10% TW, which verifies the fact that the circumferential channel is more sensitive to the circumferential defects than the axial channel. For the ID circumferential defects, the POD curve of the TMR array probe is below the POD curves of the coil array probe. This is because the eddy current induced by the TMR array probe flows circumferentially in the TW. Therefore, circumferential defects do not disturb the distribution of the eddy current as much as axial defects with similar dimensions, resulting in that the TMR array probe is not as sensitive to circumferential defects as axial defects. For the OD circumferential defects, the POD curve of the coil array probe is below the POD curve of the TMR array probe. This is because the excitation frequency of the TMR is lower than the coil array probe, resulting in larger penetration depth which is more suitable for far-side defects inspection.

4 Model-Based POD Calculation Method with Parameters from Experiment

It is expensive and time consuming to obtain POD curves experimentally. An alternative approach is using numerical model to estimate POD of a probe. However, it is difficult to achieve reasonable assumptions about the parameters in the numerical calculation. To figure out this problem, this paper proposes a model-based POD (MPOD) calculation method with parameters obtained from experiment.

4.1 Numerical Model

Three-dimensional (3D) finite element method (FEM) models were built to calculate the responses of the TMR array probe and the coil array probe. The geometry dimensions and material properties in the numerical model are similar as that in the experiment. The governing equation of the FEM model is the reduced magnetic vector potential (RMVP) formulations [5]. According to the RMVP formulation, the magnetic vector potential (MVP) due to current source and the source magnetic field intensity were calculated analytically at each scan point. The coil array probe consists of two rows of 16 pick-up coils. The center distance of the two rows of coils is 6 mm. The OD of the coil array is 16 mm. The OD, ID, height of the pick-up coil in the coil array probe are 2.6 mm, 0.5 mm and 0.5 mm, respectively. The number of turns of each coil is 100. The OD, ID, height and number of turns of the TMR excitation coil are 16 mm, 15.8 mm, 8 mm and 200, respectively.

The simulation models for the two probes are presented in Fig. 14, where the surrounding air is not shown. The dimensions of the steam generation tube are 30 mm in length, 19.04 mm in OD and 16.86 mm in ID. The conductivity and relative permeability of the tube are 8.7×10^5 S/m and 1 respectively. The conductivity and relative permeability of the air are 0 S/m and 1 respectively. The number of elements, nodes, Dirichlet nodes of the model are 247104, 254849 and 15290, respectively.

With the FEM model, the magnetic vector potential $\boldsymbol{A}$ at each node position was numerically solved. Then, the magnetic fields at the locations where the TMR array sensors were located were calculated as Eq. (4).

$$\begin{aligned} \boldsymbol{B} &= \nabla \times \boldsymbol{A} \\ \boldsymbol{B}_r &= \boldsymbol{B}_x \cos\theta + \boldsymbol{B}_y \cos\theta \end{aligned} \tag{4}$$

where $\boldsymbol{B}$ is magnetic flux density, $\boldsymbol{B}_x$ and $\boldsymbol{B}_y$ is the x- and y-component of $\boldsymbol{B}$, θ is the angle of the observation point depart from the x-axis and $\boldsymbol{B}_r$ is the radial component of $\boldsymbol{B}$.

For the coil array probe, the induced voltages (V) of the pick-up coils were calculated as Eq. (5).

$$V = -j\omega N \oint \boldsymbol{A} d\boldsymbol{l}, \tag{5}$$

where N is the number of turns of the coil, the loop integration is along the circumference of the coil.

4.2 Model Validation

To make the numerical results comparable with the corresponding experimental signals, the simulated results need to be calibrated. The amplitude and phase difference between the simulated signals and the experimental signals were calculated. Then two parameters, namely amplitude factor (α) and phase angle (θ) were obtained. The calibration of a signal was nothing but multiplying the phasor domain signal with a complex number $\alpha e^{j\theta}$. In this study, the signal of the ID defect with depth 60% TW was utilized to calculate the calibration factors. Figure 15 shows the comparison of the real component of the TMR array probe for the axial ID defect with depth 60% TW. Figures 16 and 17 show the comparison of the experimental and simulated results of the coil array probe for an axial ID defect and a circumferential ID defect with depth 60% TW. It is seen that the simulated results are similar to their corresponding experimental images, and the calibrated simulated results are comparable with the experimental signals quantitatively. These results validate the numerical model.

4.3 Calculation of POD Curves Based on Numerical Model

The flow chart of MPOD calculation method with parameters obtained from experiment is as shown in Fig. 18. Firstly, a group of defects with different dimensions are calculated based on the simulation model resulting in a group of simulated data for POD calculation. Next, the features of the signals, e.g., peak value of its amplitude V_p, are extracted. In parallelly, a typical defect is repeatedly inspected by the probe with different operators at different time. The defect with depth 60% of the TW is selected in this study. It is worth noting that other defects are also feasible as long as the signal-to-noise ratio of the signal is sufficient to extract the features accurately. Then the simulated results are calibrated according to the experimental results. It is assumed that the unknown variation in a real sample would affect both probes in the same manner. The distribution characteristics of the experimental results are calculated, which are then applied to the simulated results to generate data with normal distribution. So, a PDF is generated for each depth. Finally,

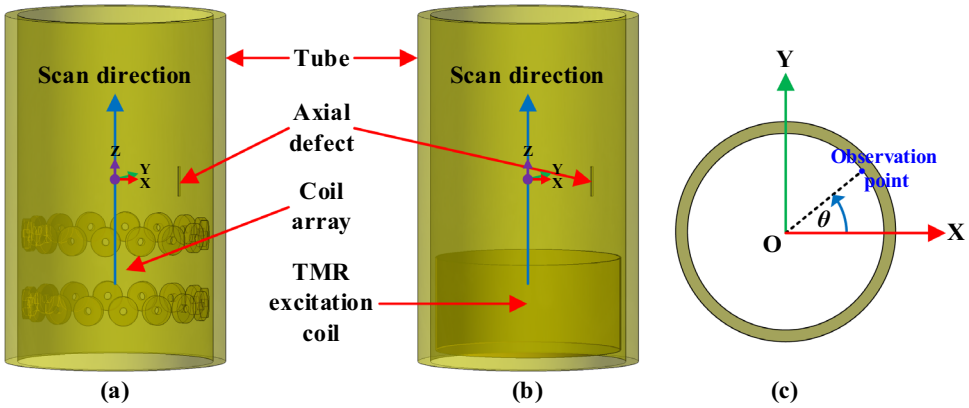

Fig. 14 Simulation model: **a** schematic showing the tube and the coil array probe, **b** schematic showing the tube and the excitation coil of the TMR probe, and **c** top view of the tube

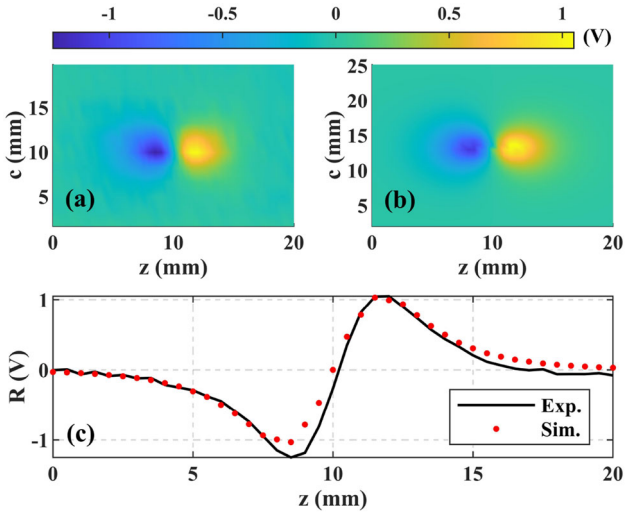

Fig. 15 Comparison of the real component of the TMR array probe for the axial ID defect with depth 60% TW: **a** experimental image, **b** simulated image and **c** line plots along the z-axis through the center of the defect

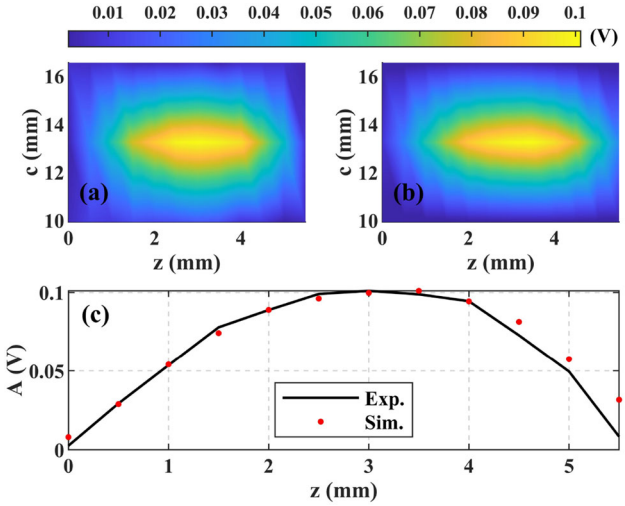

Fig. 16 Comparison of the amplitude of the Coil-A for the axial ID defect with depth 60% TW: **a** experimental image, **b** simulated image and **c** line plots along the z-axis through the center of the defect

the POD curve is obtained according to Eq. (3) with a set threshold value.

5 Results and Discussion

To validate the method of calculating POD curve based on simulation and experiment, the POD curves calculated with this method were compared with the POD curves obtained from the experimental data, as shown in Figs. 19 and 20. Here the solid line and dashed line curves are calculated based on experimental data and MPOD respectively. These curves cover the comparison of the axial, circumferential, ID and OD defects detection capabilities of the two probes.

As demonstrated before, the TMR array probe has better detectability for axial defects than circumferential defects. Therefore, the POD curves of the TMR array probe for ID and OD axial defects calculated based on the MPOD method are compared with the experimental curves in Fig. 19.

For circumferential defects, Coil-C image of the coil array probe has better performance than the Coil-A. Thus, the POD curves of Coil-C and the TMR array probe are selected to be compared in Fig. 20 for circumferential ID defects. It is confirmed that the coil array probe is better for inspection of circumferential defects than the TMR array probe. It is seen that the POD curves calculated with MPOD are similar with the curves obtained from experiment. The average error between the experimental POD curves and MPOD curves are 1.04% and 0.66% for the TMR array probe and coil array probe respectively, which validates the method.

It should be noted that the POD curve calculation based on MPOD only needs experimental results of one defect, which significantly reduced the cost of preparing samples. In addition, as the simulated results are calibrated according to the experimental results and the statistical characteristics

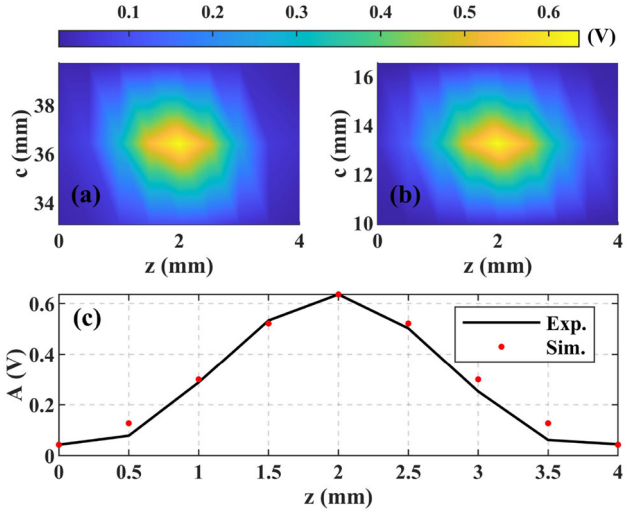

Fig. 17 Comparison of the amplitude of the Coil-C for the circumferential ID defect with depth 60% TW: **a** experimental image, **b** simulated image and **c** line plots along the z-axis through the center of the defect

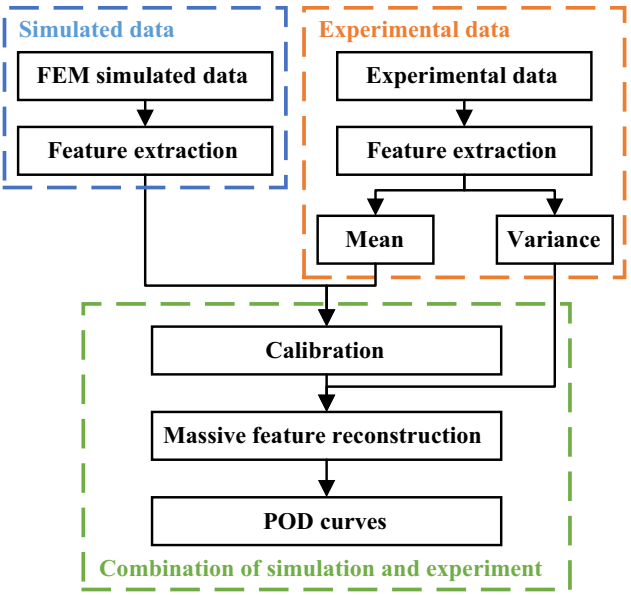

Fig. 18 Flow chart of calculating POD curve based on model-based POD with parameters obtained from experiment

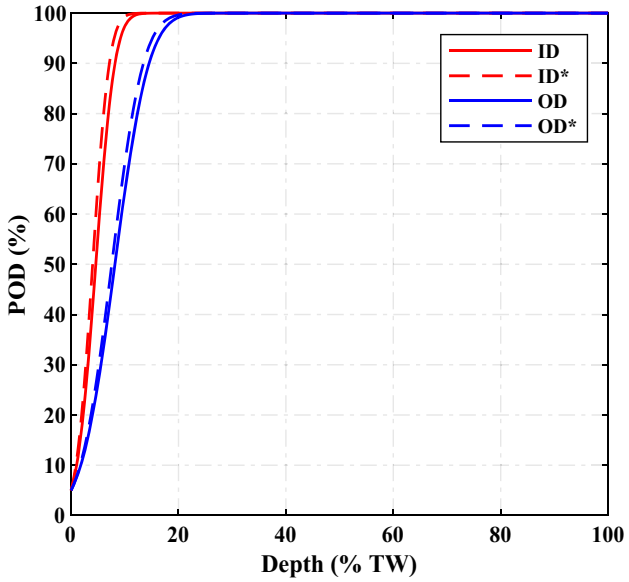

Fig. 19 POD curves calculated based on experimental data and MPOD of the TMR array probe for axial defects. Here the solid line curves are calculated from experimental data and the dashed curves are obtained with MPOD (marked by *)

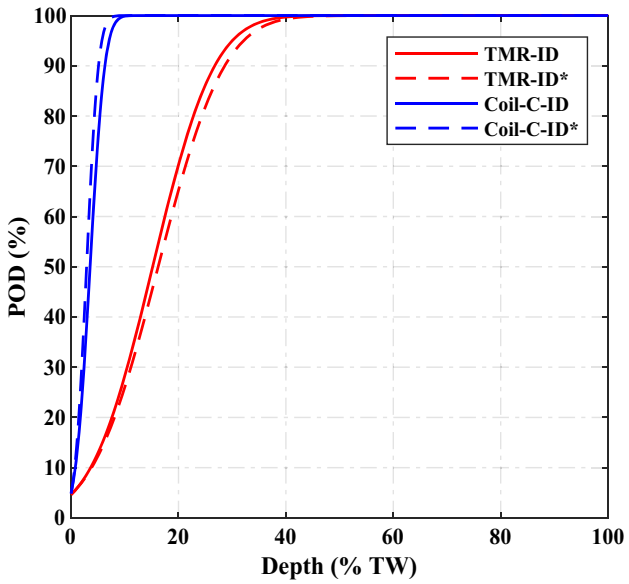

Fig. 20 POD curves calculated based on experimental data and MPOD of the coil array probe and TMR array probe for circumferential ID defects. Here the solid line curves are calculated from experimental data and the dashed curves are obtained from MPOD (marked by *)

of the signal are obtained from the repeated experiments, uncertain parameter choices are avoided. Therefore, the POD curves obtained with this method are more accurate than the purely numerical method. In the future, this method may be employed to compare the performance of different probes and optimize the parameters of a probe efficiently and economically.

6 Conclusion

Two array probes for SGT inspection, namely a TMR array probe and a coil array probe, are compared based on POD evaluation in this paper. The TMR array probe consists of 32 sensors that were placed inside a 3D printed plastic structure. An excitation cylindrical coil was wounded outside of

the sensors to induce eddy currents in the TW. The coil array probe consists of two rows of coils and each row has 16 coils that cover the full circumference of inner tube surface. The coil array probe works in transmit-receive mode with two sets of images (Coil-A and Coil-C) obtained. A SGT sample with machined defects was inspected by the probes repeatability with multiple sets of images obtained, from which the POD curves of the probes for different kinds of defects were calculated and quantitatively compared. It was derived from the POD curves that the TMR array probe has the best performance for detection of axial oriented OD defects. For axial defects that are located ID of the TW, the two probes have comparable detectability. The axial channel of the coil array probe is much more sensitive to axial defects than the circumferential channel, and the circumferential channel of the coil array probe is much more sensitive to circumferential defects. For the circumferential ID defects, the POD curve of the TMR array probe is lower than the POD curves of the coil array probe. This is because the eddy current induced by the TMR array probe flows circumferentially in the TW. Therefore, the excitation method of the TMR array probe is desired to be optimized to achieve better sensitivity for circumferential defects.

As it is expensive and time consuming to obtain POD curves experimentally, a MPOD calculation method with parameters obtained from experiment was proposed in this paper. Only one defect needs to be repeatedly tested by the probe experimentally. Then the distribution characteristics of the experimental results were calculated. Sufficient simulated data for defects with different dimensions was calculated numerically. The simulated results were calibrated according to the experimental results. Next, the distribution characteristics calculated from the experimental results were applied to the numerical results to generate data with certain probability distribution. Lastly, POD curves were calculated from the data. This method avoids uncertain parameter choices of calculating POD curves based on numerical model. The method is validated by comparing the calculated POD curves of the array probes to the experimental curves. It is found that the average error between the experimental POD curves and MPOD curves are 1.04% and 0.66% for the TMR array probe and coil array probe respectively. MPOD can be employed to compare different probes and optimize the parameters of a probe efficiently and economically in the future.

Acknowledgements This work is sponsored by Shanghai 2020 "Science and Technology Innovation Action Plan" Scientific Instrument Field Project 20142200200.

References

1. Sedighi, M., Ghasemi, M., Mohammadi, M., Hassan, S.H.: A novel application of a neuro-fuzzy computational technique in modeling of thermal cracking of heavy feedstock to light olefin. RSC Adv. **4**, 28390–28399 (2014). https://doi.org/10.1039/C4RA02392G
2. Xin, J.: Design and analysis of rotating field eddy current probe for tube inspection (2014). https://d.lib.msu.edu/etd/2542. Accessed 9 Dec 2021
3. Hur, D.H., Choi, M.S., Lee, D.H., Kim, S.J., Han, J.H.: A case study on detection and sizing of defects in steam generator tubes using eddy current testing. Nucl. Eng. Des. **240**, 204–208 (2010). https://doi.org/10.1016/j.nucengdes.2009.10.006
4. Yuan, X., Li, W., Chen, G., Yin, X., Ge, J., Jiang, W., Zhao, J.: Bobbin coil probe with sensor arrays for imaging and evaluation of longitudinal cracks inside aluminum tubes. IEEE Sens. J. **18**, 6774–6781 (2018). https://doi.org/10.1109/JSEN.2018.2842090
5. Ye, C., Zhang, N., Peng, L., Tao, Y.: Flexible array probe with in-plane differential multi-channels for inspection of micro-defects on curved surface. IEEE Trans. Ind. Electron. (2021). https://doi.org/10.1109/TIE.2021.3050376
6. She, S., Liu, Y., Zhang, S., Wen, Y., Zhou, Z., Liu, X., Sui, Z., Ren, D., Zhang, F., He, Y.: Flexible differential butterfly-shape eddy current array sensor for defect detection of screw thread. IEEE Sens. J. **21**, 20764–20777 (2021). https://doi.org/10.1109/JSEN.2021.3093550
7. Zhao, Y., Qi, P., Xie, Z., Bai, P., Chen, H.-E., Xie, S., Liao, S., Chen, Z.: A new array eddy current testing probe for inspection of small-diameter tubes in Tokamak fusion devices. Fusion Eng. Des. **157**, 111627 (2020). https://doi.org/10.1016/j.fusengdes.2020.111627
8. Xie, L., Gao, B., Tian, G.Y., Tan, J., Feng, B., Yin, Y.: Coupling pulse eddy current sensor for deeper defects NDT. Sens. Actuators Phys. **293**, 189–199 (2019). https://doi.org/10.1016/j.sna.2019.03.029
9. Sun, Z., Cai, D., Zou, C., Zhang, W., Chen, Q.: Design and optimization of a flexible arrayed eddy current sensor. Meas. Sci. Technol. **28**, 045105 (2017). https://doi.org/10.1088/1361-6501/aa5b76
10. Zhang, N., Ye, C., Peng, L., Tao, Y.: Eddy current probe with three-phase excitation and integrated array tunnel magnetoresistance sensors. IEEE Trans. Ind. Electron. **68**, 5325–5336 (2021). https://doi.org/10.1109/TIE.2020.2989704
11. Mu, X.-H., Liu, H.-F., Tong, Z.-Y., Du, B., Liu, S., Liu, B., Liu, Z.-W., Gao, C., Wang, J., Dong, H.: A new rapid detection method for ricin based on tunneling magnetoresistance biosensor. Sens. Actuators B **284**, 638–649 (2019). https://doi.org/10.1016/j.snb.2018.12.127
12. Caetano, D.M., Rabuske, T., Fernandes, J., Pelkner, M., Fermon, C., Cardoso, S., Ribes, B., Franco, F., Paul, J., Piedade, M., Freitas, P.P.: High-resolution nondestructive test probes based on magnetoresistive sensors. IEEE Trans. Ind. Electron. **66**, 7326–7337 (2019). https://doi.org/10.1109/TIE.2018.2879306
13. Tao, Y., Peng, L., Li, X., Ye, C.: Eddy current probe with integrated tunnel magnetoresistance array sensors for tube inspection. IEEE Trans. Magn. **56**, 1–8 (2020). https://doi.org/10.1109/TMAG.2020.2981435
14. Warren, A., Heslehurst, R., Wilson, E.: Composites and MIL-STD-1530C. Int. J. Struct. Integr. **5**, 2–16 (2014). https://doi.org/10.1108/IJSI-02-2013-0002
15. Mueller, C., Bertovic, M., Pavlovic, M., Kanzler, D., Ewert, U., Pitkänen, J., Ronneteg, U.: Paradigm shift in the holistic evaluation of the reliability of NDE systems. Mater. Test. **55**, 261–269 (2013). https://doi.org/10.3139/120.110433
16. Holstein, R., Bertovic, M., Kanzler, D., Müller, C.: NDT reliability in the organizational context of service inspection companies. Mater. Test. **56**, 607–610 (2014). https://doi.org/10.3139/120.110601
17. Jarvis, R., Cawley, P., Nagy, P.B.: Performance evaluation of a magnetic field measurement NDE technique using a model assisted

Probability of Detection framework. NDT E Int. **91**, 61–70 (2017). https://doi.org/10.1016/j.ndteint.2017.06.006
18. Bato, M.R., Hor, A., Rautureau, A., Bes, C.: Experimental and numerical methodology to obtain the probability of detection in eddy current NDT method. NDT E Int. **114**, 102300 (2020). https://doi.org/10.1016/j.ndteint.2020.102300
19. Calmon, P., Jenson, F., Reboud, C.: Simulated probability of detection maps in case of non-monotonic EC signal response. AIP Conf. Proc. **1650**, 1933–1939 (2015)
20. Li, M., Meeker, W.Q., Thompson, R.B.: Physical model-assisted probability of detection of flaws in titanium forgings using ultrasonic nondestructive evaluation. Technometrics **56**, 78–91 (2014). https://doi.org/10.1080/00401706.2013.818580
21. Annis, C.: MIL-HDBK-1823A. Nondestructive Evaluation System. Reliability Assessment Department Defence Handbook. Wright-Patterson AFB, Dayton (2009)
22. Zhu, J., Min, Q., Wu, J., Tian, G.Y.: Probability of detection for eddy current pulsed thermography of angular defect quantification. IEEE Trans. Ind. Inform. **14**, 5658–5666 (2018). https://doi.org/10.1109/TII.2018.2866443
23. Le Gratiet, L., Iooss, B., Blatman, G., Browne, T., Cordeiro, S., Goursaud, B.: Model assisted probability of detection curves: new statistical tools and progressive methodology. J. Nondestruct. Eval. **36**, 8 (2017). https://doi.org/10.1007/s10921-016-0387-z
24. Rosell, A.: Finite element modelling of eddy current nondestructive evaluation in probability of detection studies (2012). https://publications.lib.chalmers.se/records/fulltext/156770.pdf. Accessed 6 Dec 2021
25. Zeng, Z.: Applications of POD studies and robust design to electromagnetic NDE (2003). https://lib.dr.iastate.edu/rtd/1408. Accessed 2 June 2021

Publisher's Note Springer Nature remains neutral with regard to jurisdictional claims in published maps and institutional affiliations.